Natural Hazards (2026) 122:285
https://doi.org/10.1007/s11069-026-07989-y

ORIGINAL PAPER

An evaluation of near-surface sediments enhancing ground motions excited by shallow local earthquakes near Union City, Oklahoma

John McKnight[1] · Paul Ogwari[2] · Jacob I. Walter[2] · Raymond Ng[1] · Danial Mansourian[1] · Sina Saneiyan[3]

Received: 23 December 2024 / Accepted: 13 January 2026

Abstract
Hydraulic fracturing activities and the subsequent wastewater injection into the subsurface have increased the number of felt seismicity in Oklahoma. Some of the smaller magnitude ($M < 3.5$) earthquakes have been associated with reported damage to the built environment. We evaluate the subsurface structure of the near-surface sediments in Union City, Oklahoma to identify and delineate subsurface structures that amplify ground motion in the area. The study area is adjacent to the Canadian River, a major braided meandering river that traverses Oklahoma generally from west to east, that has significant alluvial depositions that are visible near roadways and from aerial imagery. We analyzed ambient noise data from 60 continuously-recording seismic nodes as well as approximately two kilometers of electrical resistivity tomography (ERT) and induced polarization (IP) data. We performed horizontal-vertical spectral ratio (HVSR) to deduce the dominant resonant frequencies and paired the resonant frequency information with the higher resolution ERT to resolve the sedimentary structures that produce the observed resonance. Our analysis indicates that the higher resonance frequencies are found further away from the riverbanks, and the inverted depth matches the depth and thickness of the mapped terrace deposits in the area. In the southern area, closer to the riverbank, the dominant resonant frequencies are controlled by thick clay layers that are deeper than the alluvial deposits from the Canadian river. The lower frequency resonance corresponds to the depths where the transition between Permian and Pennsylvanian deposits produce high impedance contrast at the strata boundaries resulting in amplified ground motion.

Keywords Earthquake · Passive Seismic · Electrical Resistivity · Induced Polarization · HVSR · Induced Seismicity · Wastewater Injection · Horizontal-Vertical Spectral Ratio

✉ Sina Saneiyan
ssaneiyan@binghamton.edu

[1] School of Geosciences, University of Oklahoma, Norman, OK, USA

[2] Oklahoma Geological Survey, University of Oklahoma, Norman, OK, USA

[3] Department of Earth Sciences, Binghamton University, Binghamton, NY, USA

Published online: 06 March 2026

1 Introduction

The practice of horizontal drilling, combined with fluid injection into subsurface cracks for oil extraction, commonly known as hydraulic fracturing or fracking, has been identified as a common source of induced seismicity in Oklahoma (Hincks et al. 2018; Ries et al. 2020; Zhai et al. 2019). Injection of fluids into the deep subsurface initiates stress and pore pressure changes within hydrocarbon host rock (Eaton and Schultz 2018) and, in some cases, causes reactivation of existing faults (Schoenball and Ellsworth 2017). Historically, active fault zones have produced earthquakes in central and southern Oklahoma but the surge in wastewater injection from oil and gas production has triggered activity in previously dormant fault systems across the state thereby increasing the rate of seismicity by 30 fold by mid 2016 (McNamara et al. 2015). To date, Oklahoma's induced seismic activity has decreased due to implementation of new regulations regarding wastewater injection (Murray et al. 2023). However, there remains significant hazard from occurrence of medium sized to smaller magnitude earthquakes ($M<3.5$) which subsequently increases risk to residential buildings in rural areas. The ground motion in Oklahoma caused by induced earthquakes ($M>3.5$) exhibits amplitudes comparable to California's natural earthquakes (Atkinson 2020). In areas with frequent earthquakes, buildings deteriorate at a high rate thereby negatively contributing to the economic welfare of the affected areas (Atkinson 2020; Cheung et al. 2018) in addition to physical damage to the built environment. In Oklahoma, there were over 3,000 moderate to small magnitude earthquakes (i.e., $M<3.5$) recorded during the calendar year 2022. During that time period, only two induced earthquakes with $M>3.5$ were recorded (USGS Earthquake Catalog 2024). In general, earthquakes damage to structures depends on the structure size, age, and other seismogenic factors such as proximity to the recorded earthquakes (Taylor et al. 2018). Such damages, for instance drywall cracking on residential buildings, have been widely reported in Union City, OK, an area that has experienced frequent small magnitude earthquakes from hydraulic fracturing activities. In most cases, the small magnitude earthquakes may not be felt by people, but surface resonance has been observed to produce ground motions and amplified amplitudes relative to similarly sized earthquakes in other regions, as previously reported (Ogwari et al. 2022). This has been demonstrated to have the effect that earthquake magnitudes that are typically not felt may reach perceived intensities that observers report feeling such ground motions. Union City is located about one mile north of the Canadian River in central Oklahoma where the near surface sediments are heterogenous due to several depositional episodes following the change of the river course since at least the start of the Holocene. The layered alluvial deposits have previously been suggested to be the source of seismic energy amplification (Walter et al. 2019).

We evaluate the near surface sediments to determine the source of the ground motion amplification near Union City. We conduct a small geophysical study crossing a transition of the river deposits and evaluate their response to seismic energy in order to understand their contribution to ground motion amplification in the area. We use electrical resistivity tomography (ERT), induced polarization (IP) and passive seismic to characterize the near surface region (depth < 100 m). The ERT and IP surveys provide continuous and high-resolution imaging of the near surface horizons (compared to passive seismic surveys) which can relay lithologic information about subsurface sediments, especially when paired with in-situ ground truthing. On the other hand, the horizontal-vertical spectral ratio (HVSR)

from the passive seismic identifies and characterizes zones of resonance at greater depths, thereby mapping horizons that the ERT and IP surveys are limited by the survey setup. Although HVSR's horizontal resolution, limited by seismometer spacing, is less than ERT and IP, it has the capacity to provide details about deep subsurface horizons (Mulargia and Castellaro 2016). All methods utilized are inherently non-invasive; therefore, they do not negatively impact the environment. Moreover, the methods can monitor seismic activity while studying the near surface sediments at a large scale (~2 km). These methods, as combined, synergistically delineate the subsurface structures that amplify the ground motion in Union City.

2 Study area

The study area is located in southwest of Oklahoma City, Oklahoma, USA (red square in Fig. 1). Soil types include intermittent clayey soils intertwined with sandy or silty soils within the first few meters of the subsurface (Carter and Gregory 2008). Surficial geologic deposits in the areas mainly consist of alluvium, terrace deposits, and Dog Creek shale (Curtis 2003). The alluvium in Canadian County averages about 15 m in depth and has intermittent lenses of clay and silt (Breit et al. 2008; Tuttle et al. 2009) and, with depth, becomes increasingly sandy (Havens 1989; Moreno 2012; Tuttle et al. 2009). Often adjacent to the alluvium deposits are terrace deposits which are Pleistocene in age (Curtis 2003) and have lenticular bedding with similar grains size variations as the alluvium (*Geologic Units in Canadian County*, *Oklahoma*, 2024). The oldest sediments in the study area are primarily shales, such as the Dog Creek shale and the Oscar Group, that are Permian and Pennsylvanian in age, respectively (*Geologic Units in Canadian County*, *Oklahoma*, 2024).

3 Methods

3.1 Electrical resistivity tomography and induced polarization

The direct current (DC) electrical resistivity method is based on the conduction of electrical current in materials according to Ohm's law. In ERT surveys, current is transmitted through the media at two current electrodes and the voltage drop is measured across two potential electrodes. By knowing the geometry of the electrode configuration, the apparent resistivity (ρ_a – Ωm) is calculated as,

$$\rho_a = K \times R = K\frac{\Delta V}{I} \tag{1}$$

where R is resistance (Ω), ΔV is potential drop (V), I is current (A), and K (m) is the geometric factor.

In heterogeneous media, the resistivity (ρ) is determined from an inversion process (see Binley and Slater 2020 for a review). Here we used the open-source geoelectrical modeling and inversion software, ResIPy (Blanchy et al. 2020; Boyd et al. 2019). ρ is independent of the measurement setup and is an intrinsic property of the medium. In near-surface soils

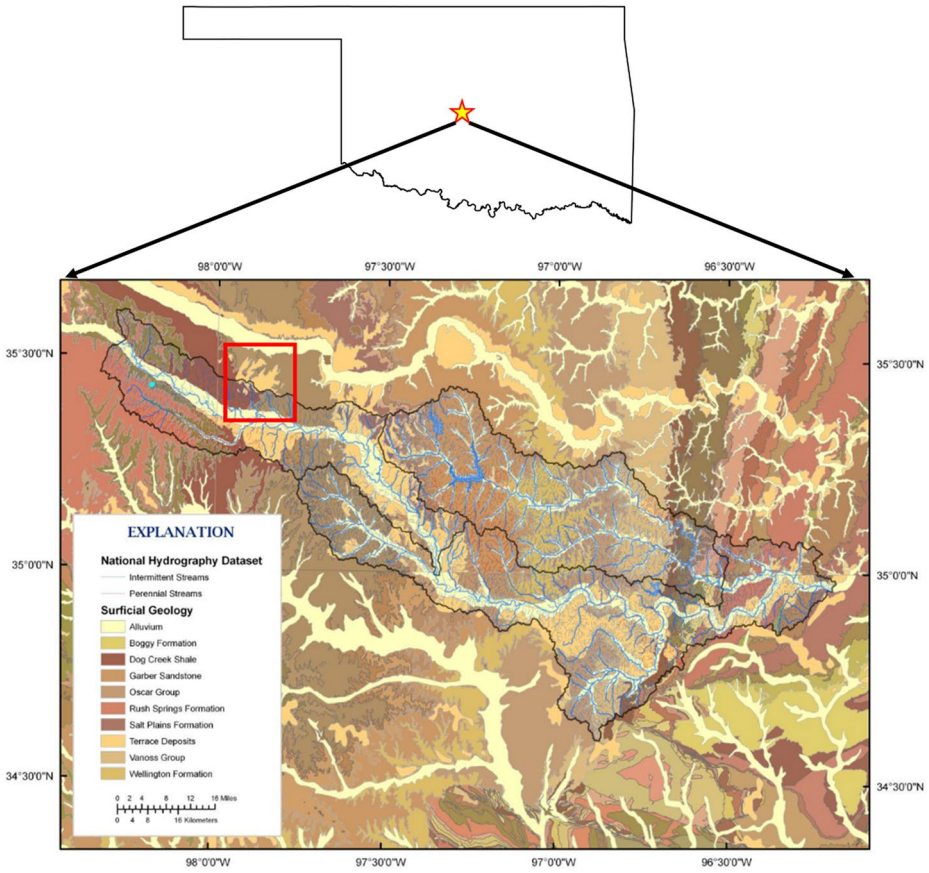

Fig. 1 A geological map of surficial deposits and outcrops in southwest-central Oklahoma (from Moreno 2012) showing the study area (the red square). The blue lines trace the stream tributaries flowing into the Canadian River

where electronic conductors (e.g., metals) are typically absent, electrical current travels through parallel electrolytic and surface ionic pathways (Waxman and Smits 1968). Thus, ρ depends on many textural characteristics of soil such as porosity, tortuosity, and surface area (Kemna et al. 2012) which results in signal ambiguity. To overcome signal ambiguity, ERT surveys are usually accompanied by IP surveys. IP surveys are commonly performed in the time domain (TDIP) and the measured parameter is apparent chargeability (m_a – mV/V),

$$m_a = \frac{V_s}{V_p} \tag{2}$$

where V_s is the measured secondary voltage at time t after current shut-off and V_p is the primary voltage (current is on). In practice, measuring V_s is difficult; therefore, m_a is measured over the voltage decay curve during time t when the current is shut off (Eq. 3),

$$m_a = \frac{1}{V_p} \int_{t1}^{t2} V_s(t)\ dt \tag{3}$$

The m_a/ρ ratio is defined as normalized chargeability (*MN*), which is mainly controlled by the ionic polarization at the grain-fluid interface and depends on specific surface area, surface ionic density and cation exchange capacity. Thus, *MN* can be used for subsurface lithological characterization (Kemna et al. 2012; Slater and Lesmes 2002a).

3.2 Passive seismic method

The HVSR technique is primarily utilized for mapping horizons using three component seismometers which record ambient noise, which are the natural reverberations within the subsurface from the seismic noise environment. In HVSR, the identification of the resonant frequencies with the most power, or peaks, are dependent on the soils and sub-surficial geology that vary in thickness, density, and gain-size (Stanko et al. 2017). The technique used in this study is based on Nakamura's method of site response analysis (Nakamura 1989, 2019; Oubaiche et al. 2016).

Larger amounts and specific frequency bands of resonance in earth material can result in enhanced ground motion at a site (Giocoli et al. 2019; Leyton et al. 2013; Stanko et al. 2017). HVSR has been traditionally utilized for seismic hazard monitoring (Mahajan et al. 2021) and building resonance (Giocoli et al. 2019); therefore, it is an adequate tool to distinguish near-surface sediment interactions with ground motion. Furthermore, buildings are engineered to withstand specific frequency band resonance, so the measurement of the earth's natural resonance is an important facet of building design.

The nodes in our study are three-component Fairfield Nodal nodes with 5 Hz natural frequency geophones that continuously record in three components, two perpendicular horizontal components and one vertical component. The ambient noise should not include human interaction, traffic induced energy, or other sources of anthropogenic surface noise as this could give false characteristic frequencies that do not reveal resonance of frequencies. Recording times vary in studies depending on the local area (a city may have few spots for nodes) and time constraints, but studies with thirty minutes of recording time (Arimuko et al. 2020) to twenty-four hours of recording time (Sivaram et al. 2018) are common. The two horizontal components are geometrically averaged and then divided by the vertical component in the frequency domain. This may produce a peak at a certain frequency depending on the study area. The peak describes the resonance frequencies at the nodal location (Fig. 2). The criteria for identifying selectable resonance frequencies were established based on comparisons with a 3-component broadband sensor installed in a nearby permanent station, O2: UCTY. The broadband sensor provided a benchmark to select resonance frequencies. Despite the nodes having an integrated low-pass filter, the instruments provide resourceful information since the HVSR method relies on the waveform ratio from the same instrument and is not adversely affected by the instrument limitation.

We utilize *Hvsrpy* (Vantassel 2021), a python package that contains the methods in Cox et al. 2020; and Cheng et al. 2020; as the primary analysis tool for the HVSR calculations in this study. The minimum and maximum frequencies after resampling were defined as 0.1–50 Hz. Resonant frequencies close to 50 Hz were identified as potentially originating from

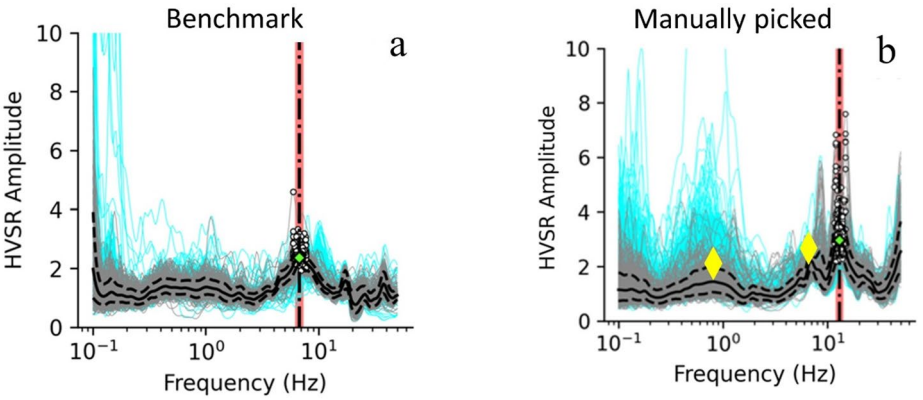

Fig. 2 An example of two resonance spectra produced using hvsrpy, including **a** benchmark spectra from a broadband seismometer at station O2: UCTY and **b** resonance spectra from a nodal sensor. The black solid curve traces the mean spectrum from the selected signal (gray), after removing noisy signal (cyan), to identify the peak resonance frequency (green diamond) selected by the algorithm. We manually picked additional resonance frequencies denoted by the yellow diamonds

unfiltered noise due to the resonant frequency picking algorithm keeping high frequency signals sourced from anthropogenic noise. Manual picking of the resonant frequencies was employed to select multiple peaks at each nodal location. Inputting the resonance frequency picks into Eq. (4), other parameters of the subsurface can be calculated.

$$f_o = \frac{Vs}{4D} \tag{4}$$

Where $f_o$is resonance frequency, V_s is shear wave velocity, and D is the thickness of the sediment body. The resonance frequency range we observed in this study (0.4–12 Hz) is high for application of ambient noise inversion of phase velocity using the nodes' configuration. We adopt a V_{s30} velocity of 560 m/s achieved by Mendoza et al. (2017) on OK01 and OK02 sites that have similar geological deposition (located ~ 50 km from study area). Mendoza et al. (2017) characterize high frequency phase velocities equivalent to the upper spectrum of the resonance frequencies achieved in our study using field-based Vs active source survey. For the lower frequencies (0.4–0.8 Hz), we used our study array to determine the phase velocities by analyzing the time moveout of the selected phases across the array through linear regression for local earthquakes located due north of the study area. The recorded waveforms are bandpass filtered between 0.6 and 0.8 Hz and analyzed for the S-wave phase travel across the N-S Nodes array recorded on the horizontal channels. We selected earthquakes with approximately zero back azimuth to eliminate the need for correction of the wavefront angle across the array. The analysis yielded a phase velocity of 1.65 km/s that we apply to invert for the resonance depths in this frequency range.

3.3 Survey setup and data processing

Six electrical survey lines (Table 1), ranging from 182 to 478.5 m, were designed (Figs. 3 and 4). ARES II resistivity meter and IRIS Syscal Terra were used to record resistivity and

Table 1 Description of each ERT/IP survey conducted, and array configurations utilized

	Length	Array configurations	Number of electrodes-spacing
Line 1	177.5 m	Dipole-Dipole, Wenner, Schlumberger, Multi-Gradient	72–2.5 m
Line 2	478.5 m	Dipole-Dipole and Schlumberger	88–5.5 m
Line 3	390.5 m	Dipole-Dipole, Schlumberger, Wenner	72–5.5 m
Line 4	478.5 m	Dipole-Dipole	88–5.5 m
Line 5	346.5 m	Dipole-Dipole, Schlumberger	64–5.5 m
Line 6	346.5 m	Dipole-Dipole, Schlumberger	64–5.5 m

IP measurements using an 850 W power output and 200 ms pulse length with stacking of 4 measurements (2% error). Dipole-Dipole, Schlumberger, and Wenner array configurations were selected based on survey time for optimal profiling (Binley and Slater 2020; Ward 1990). Electrode contact resistances were checked prior to every survey and the values were ensured to be below 50 kΩ. For each line a reciprocal data collection was conducted where the current and potential electrodes are swapped compared to the original (normal) survey (Binley and Slater 2020). Data points with higher than 10% reciprocal resistance error were filtered out prior to inversion. Furthermore, data points with extremely low current injection (< 10 mA) and measured potential (< 15 mV) were filtered out. Electrical surveys were accompanied by in-situ shallow core samplings. A manual coring device was used for collecting approximately 1-meter-long undisturbed samples up to 5 m depth. The samples were used for grain size analysis and laboratory electrical measurements.

The passive seismic setup consisted of 60 three-component nodes spaced ~ 400 m with 36 nodes in the north-south and 24 nodes in the east west direction. Passive seismic data was recorded continuously for 19 days in 24 h cycles per node. The cross-array design was chosen, in part, to investigate north-south variation in seismic velocities relative to the distance from the Canadian River. Prior to commencement of field operations, we had preliminary data suggesting ground-motions were enhanced relative to the expected shaking from similar magnitudes in this area and designated the field study area to investigate the relative variations in the shallow seismic velocity field. At the same time, the cross-array allows us to locate any small microseismicity in the area using traditional earthquake location techniques.

3.4 Laboratory testing

3.4.1 Grain size analysis

A 3 cm portion at the bottom of each core sample (representing 1 m depth intervals) was used for grain size analysis. Samples were oven-dried at 105 °C overnight. Once dried, 5 g from each sample was sieved (2 mm mesh size pan) and taken for grain size characterization. The sieved samples were mixed with a sodium hexametaphosphate solution to break down particle bonds (Hesaraki et al. 2009) and suspended clay particles were extracted and baked at 105 °C for 24 h. The remaining of the sample was sieved again with a 50 µm mesh,

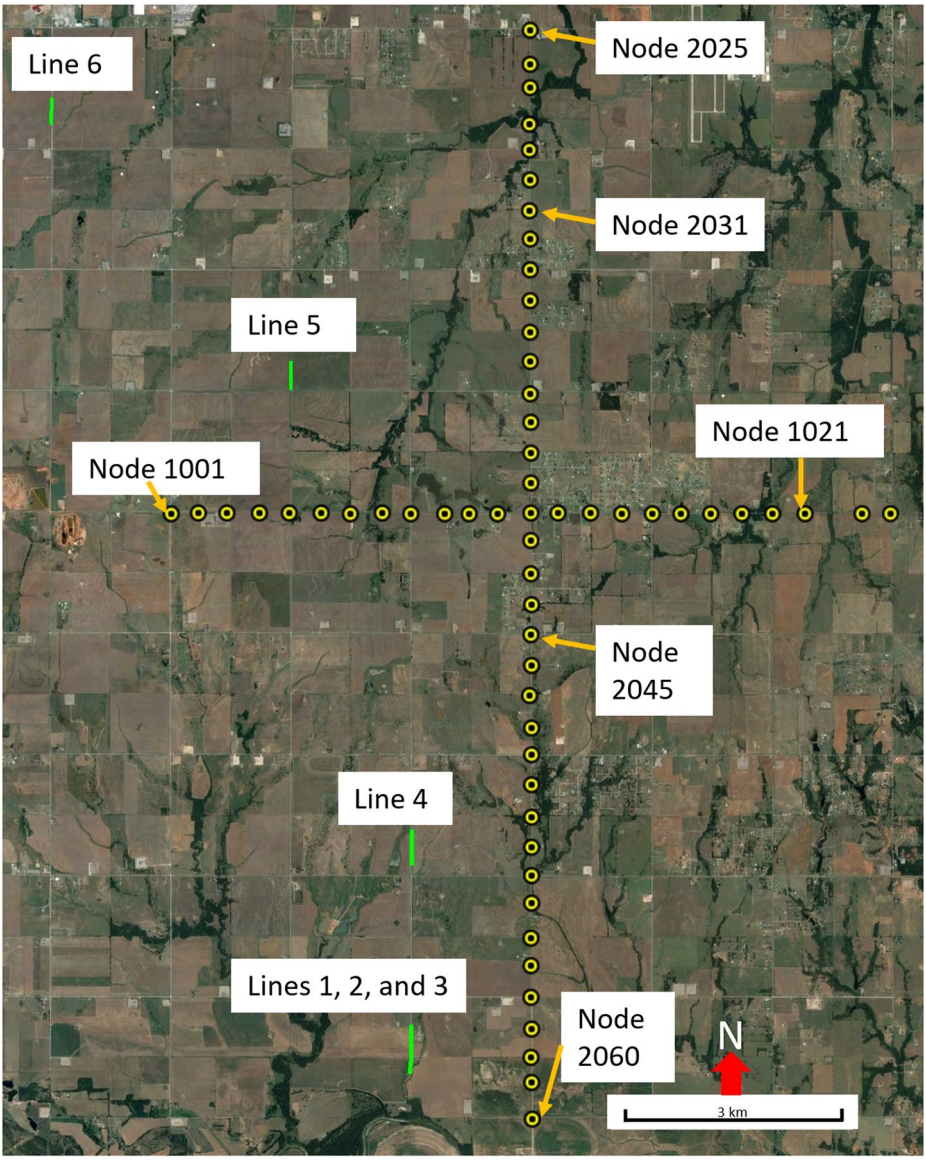

Fig. 3 Geophysical survey setup. Green lines are ERT/IP survey lines and yellow circles are passive seismic nodes. The nodes are numbered sequentially from west to east and north to south. Holocene meanders from the Canadian River (bottom of the figure) are the visible geomorphic features in the southern extent of the map

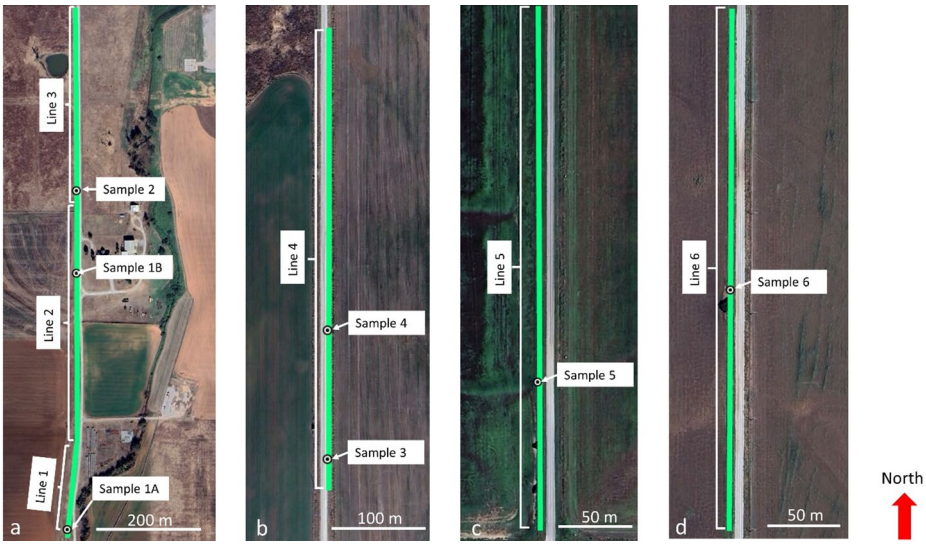

Fig. 4 ERT/IP survey lines with their respective in-situ sampling locations. **a** Lines 1–3, **b** Line 4, **c** Line 5, **d** Line 6

separating sand and silt. Sand particles were dried, and silt percentages were determined as the remaining weight difference from the original 5 g sample after accounting for the sand and clay weights.

3.4.2 Electrical measurements

Core samples retrieved from each survey line were used as ground truth for interpreting field electrical signal. A custom cylindrical sample holder was designed and equipped with two disk current electrodes at each end and two potential electrodes at the middle to ensure 1D electrical current flow in the sample, eliminating the need for inversion processes to calculate ρ (for more details see Binley and Slater 2020). All samples were packed in the sample holder in order to preserve their field conditions (e.g., the moisture content). The Ontash and Ermac portable spectral induced polarization device, operating from 10 mHz to 1 kHz was used for measuring MN and ρ of each sample.

4 Results

4.1 ERT results

Lines 1 to 3, near the Canadian River, are interconnected (collected without any gaps – Fig. 4). In Line 1, a thin (< 10 m), horizontal and resistive (30 Ωm) layer occurs at elevation 385 m (~ 7–10 m beneath the surface), overlies a less resistive layer (indicated by the red dashed lines) and appears to be reaching to the surface in Line 2 and thinning out around distance of 300 m elevation in Line 3 before completely disappearing towards the north (Fig. 5). The less resistive layer, approximately 10 m thick, extending to elevations of

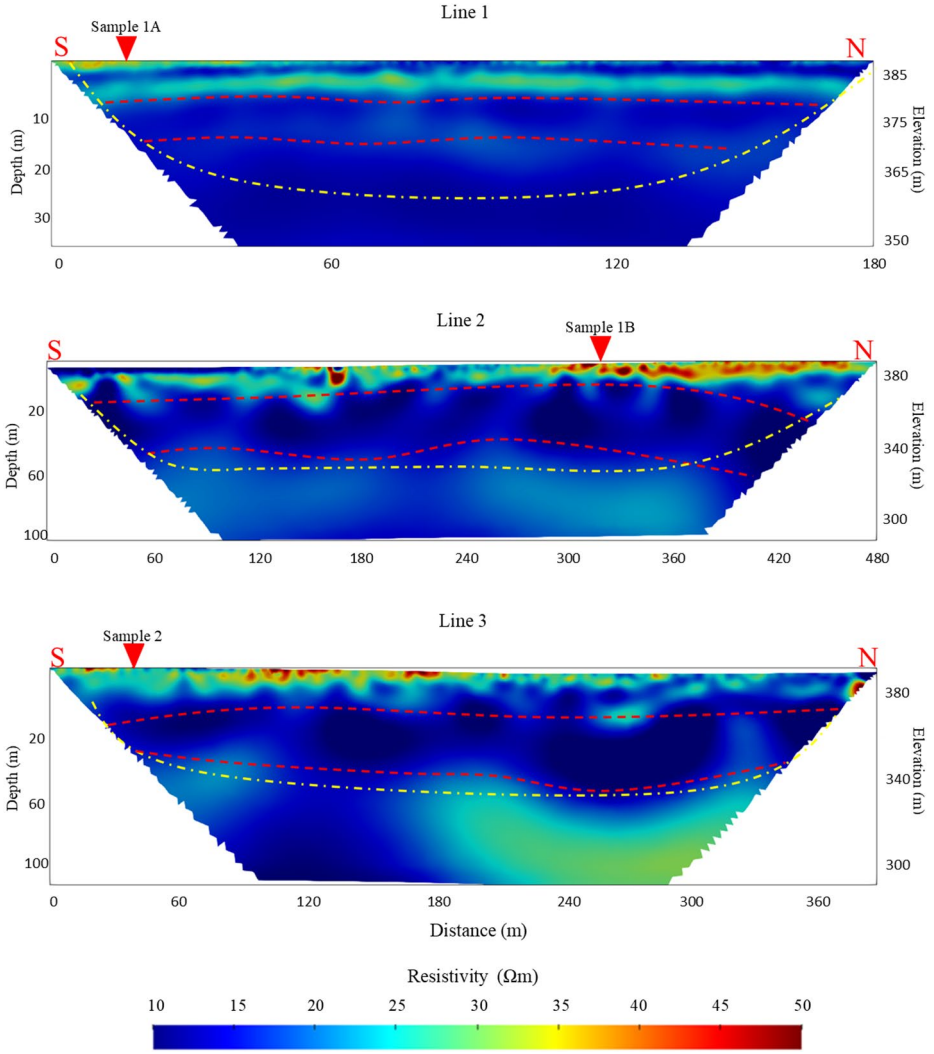

Fig. 5 A depth profile of ERT survey for Line 1, Line 2, and Line 3. The red dashed lines trace the interpreted low resistivity zones while the yellow dashed line traces the depth of investigation (DOI) for each line. The inverted red triangles at the surface of each profile mark the sampling point for grain size analysis

~370 m to ~380 m (depth of ~20 to ~30 m), continues into Line 2 and Line 3, maintaining its depth. However, it appears that this layer is getting thicker towards the end of Line 3. Line 4, located 400 m north of Line 3, is showing a similar pattern following Line 3 with a less resistive layer at elevation 370 m and no evidence of a resistive surface layer. A low resistivity (<10 Ωm) horizontal band, extending laterally at elevation of 380 m also exists here. Lines 5 and 6, located farther north (Fig. 6), both reveal a ~20 m thick resistive (>30 Ωm) layer at elevations 380 m to 410 m, maintaining a similar depth from the surface. In

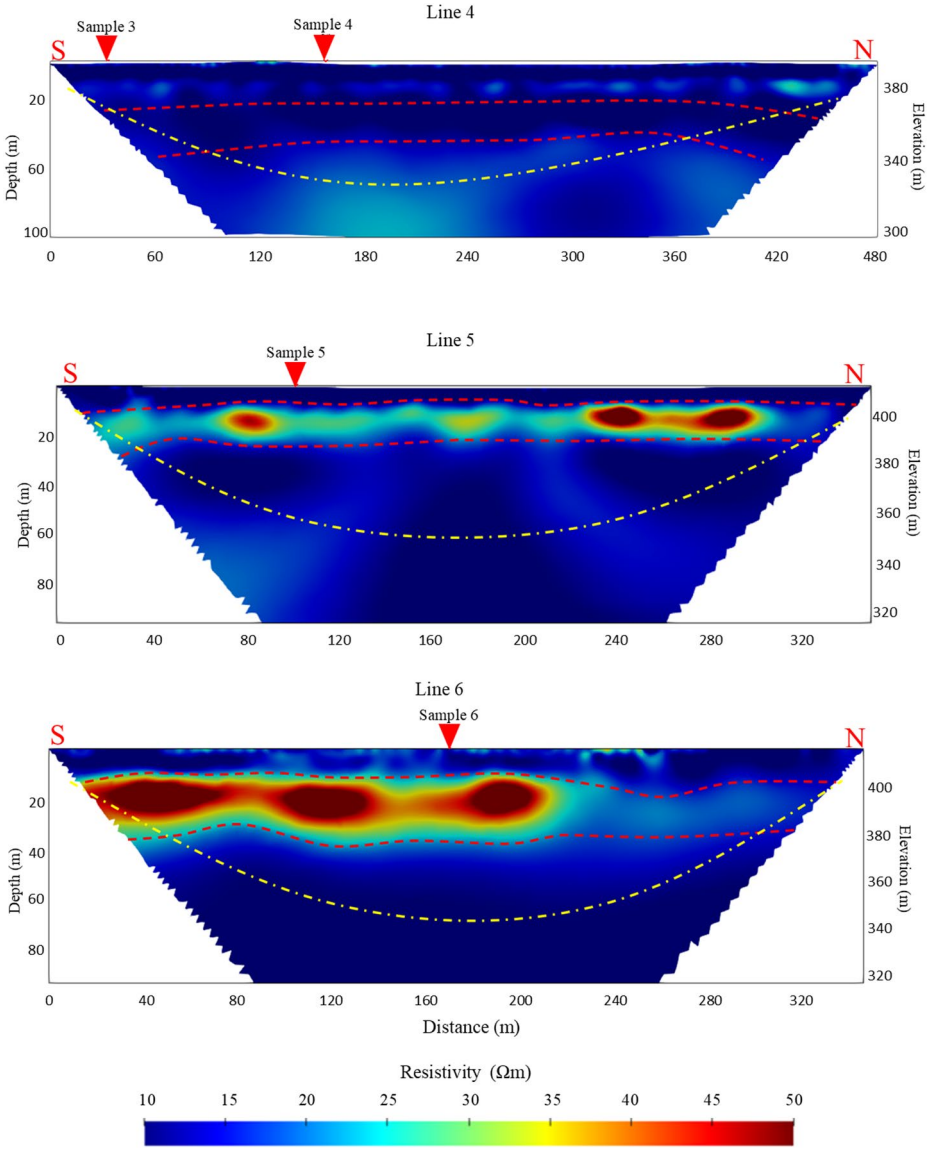

Fig. 6 A depth profile of ERT survey for Line 4, Line 5, and Line 6. The red dashed lines in Line 4 traces interpreted low resistivity zone. The red dashed Line in line 5 and 6 traces a high interpreted high resistivity zone. The yellow dashed line traces the depth of investigation (DOI) for each line. The inverted red triangles at the surface of each profile mark the sampling point for grain size analysis

both lines a thin (< 20 m thick) conductive layer, extending from surface, overlies the resistive layer.

4.2 IP results

Lines 1 to 3 show a similar *MN* pattern as their ERT results with a distinct low normalized chargeability layer occurring at 385 m elevation (depth of ~ 7–10 m beneath the surface). This layer is reaching to the surface in Line 2 but unlike the ERT results it does not get thinner with distance and maintains its thickness throughout the entire Line 3 (Fig. 7). Furthermore, Lines 1 to 3 reveal a thick (> 20 m) high normalized chargeability layer (> 15 mS/m - indicated by the red dashed lines) underlain the low chargeability layer. This layer is horizontal and maintains its depth and thickness throughout Lines 1 to 3. Similar to its ERT results, Line 4 shows a horizontal low normalized chargeability (< 50 mS/m) layer at the surface down to elevation of 380 m (Fig. 8). This layer overlies a distinct high normalized chargeability (> 50 mS/m) layer at 380 m with 20 m thickness. Line 5 and Line 6 show that surface has a high normalized chargeability. In both lines a low normalized chargeability layer exists below elevation of 400 m. This layer overlies a high normalized chargeability layer below 380 m, however at this elevation we reach to the depth of investigation limit and cannot confidently say if this layer is confirmed to be a high normalized chargeability layer or not.

4.3 Grain size analysis

Grain size analysis is crucial for correlating deeper sediments with ERT and normalized chargeability profiles. The first three samples exhibit higher clay and silt content than sand, with Sample 1 A and 1B having the highest sand content per meter. Sample 2 shows a significant decrease in sand content while having high silt levels. Sample 3 has high silt and clay compared to Samples 1 A and 2, with nearly zero sand percentage (Table 2). Sample 4, located 130 m away, has similar composition to Sample 3. Sample 5 is mainly made out of silt and clay, with some meters containing almost 50% clay. Sample 6 has the highest sand content (~ 85%) in the third meter.

4.4 Laboratory testing of the in-situ samples

Electrical results for Samples 1–3 (Fig. 5) consistently show low resistivity and high normalized chargeability, especially at Sample 1. Across all samples, there's a trend of higher chargeability correlating with lower resistivity measured in the field (at the ARES II resistivity meter's 1.25 Hz acquisition frequency). However, Sample 3 presents an abnormality where the normalized chargeability values for the first meter are greater than the third and second meters, but the first meter corresponds to a lower resistivity value compared to the second meter. This trend is observed in Samples 5 and 6 (Fig. 9) as well, where higher normalized chargeability corresponds to higher resistivity values.

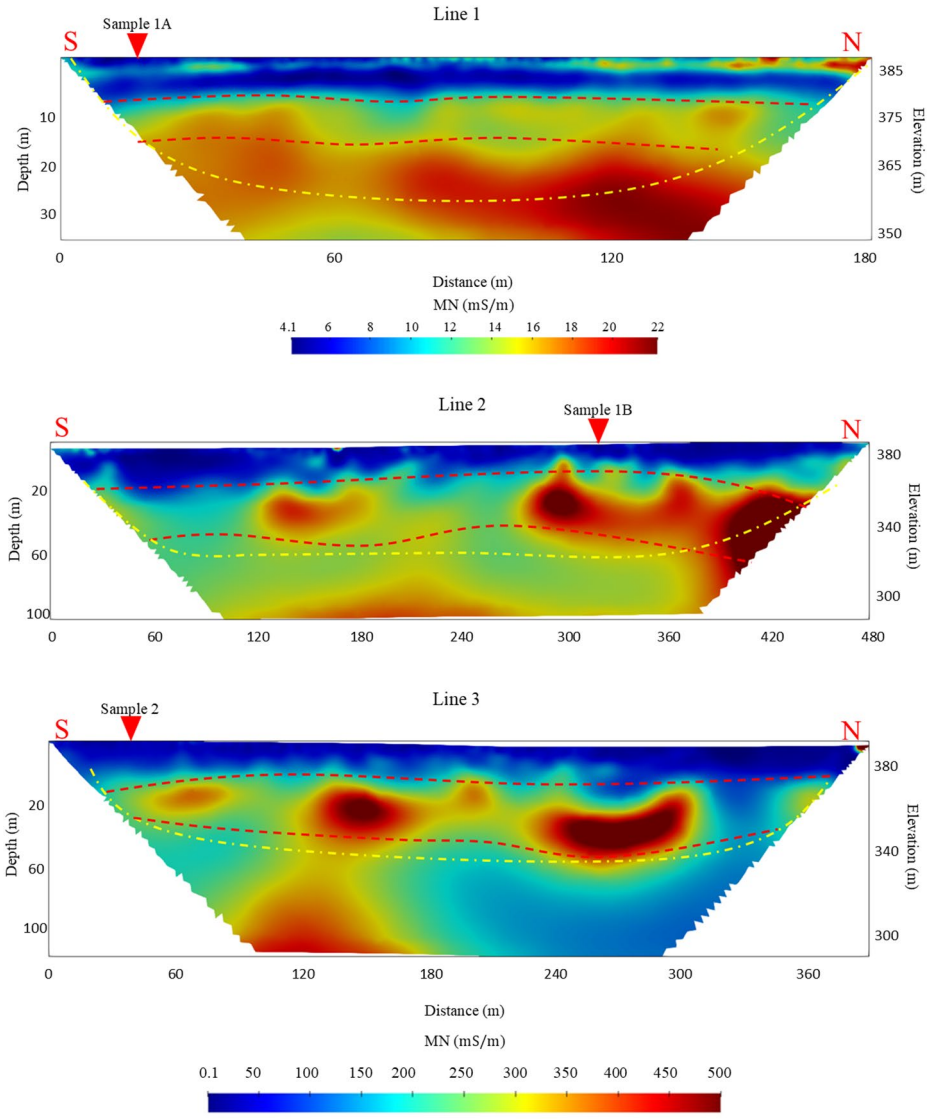

Fig. 7 The normalized chargeability depth profiles for Line 1, Line 2 and Line 3. The red dashed lines trace a zone of high normalized chargeability layer while the yellow dashed line traces the depth of investigation (DOI) for each line. Note the color scale for Line 1 is different than Lines 2 and 3 due to the significantly lower signal magnitude. The inverted red triangles at the surface of each profile mark the sampling point for grain size analysis

4.5 HVSR results from passive seismic data

The HVSR results reveal variations in two parameters: resonating frequencies of the subsurface geologic body and thickness of the stratigraphy producing the resonance inverted using Eq. (4). In the north-south node array, the resonant frequencies reveal three distinct

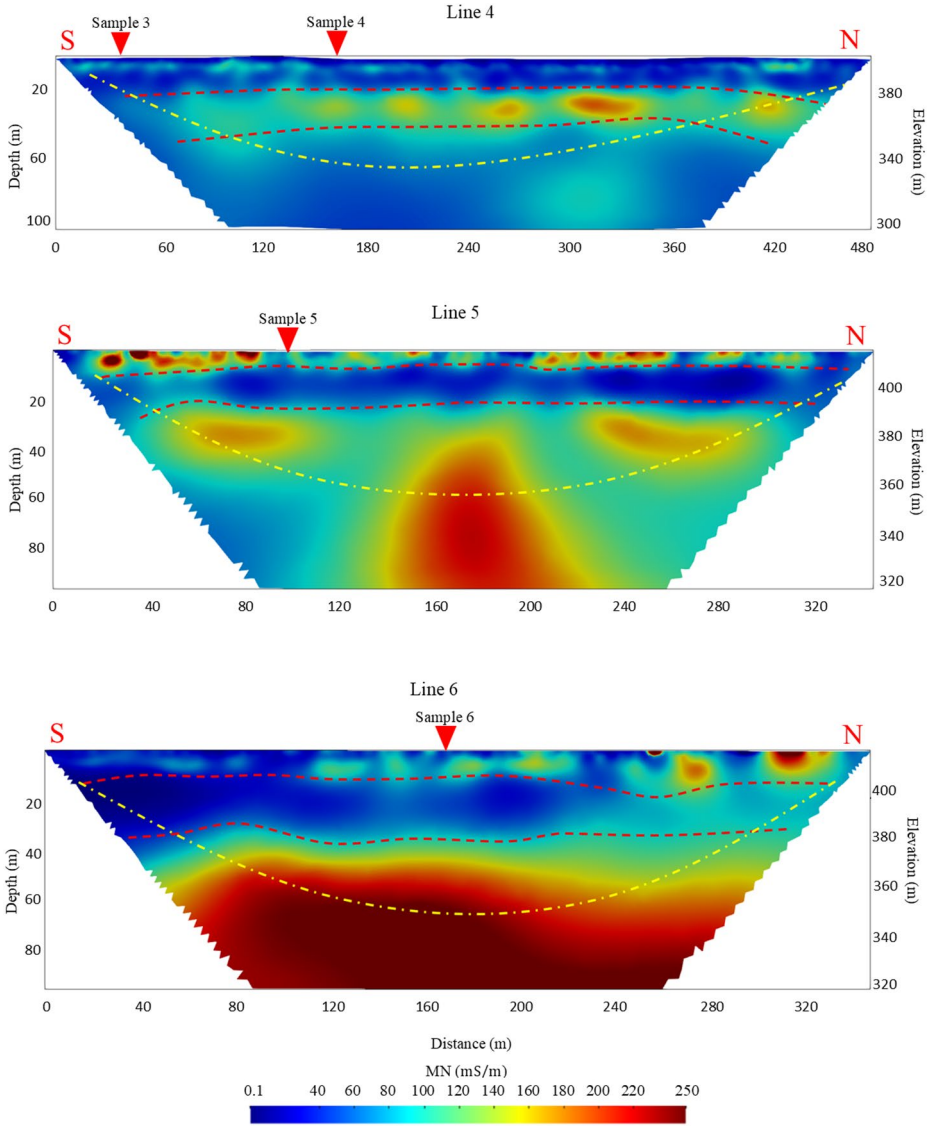

Fig. 8 The normalized chargeability depth profiles for Line 4, Line5 and Line 6. The red dashed lines trace the horizontal trends and yellow dashed line traces the depth of investigation (DOI) for each line. The inverted red triangles at the surface of each profile mark the sampling point for grain size analysis

horizons responsible for the seismic wave resonance on the north-south nodal array. We use the chargeability and resistivity inversions to guide us in tracing and extrapolating the horizons. The northern nodes have higher resonant frequency of 9 Hz (Fig. 10a), that gradually decreases southward towards the Canadian River. A second lower resonant frequency is apparent on most of the nodes except nodes ranging between 2041 and 2047. This resonance frequency has an apparent dip to the south and north of the array from the center. One more resonant frequency band is observable between 0.4 and 2 Hz (blue horizon in Fig. 10a).

Table 2 Grain size analysis results for each meter depth at all sample locations

	1st meter	2nd meter	3rd meter	4th meter	5th meter
Sample 1 A					
Sand %	5.38	37.15	55.38	40.87	
Silt %	69.52	49.80	31.47	16.27	
Clay %	25.10	13.04	13.15	41.86	
Sample 1B					
Sand %	41.63	23.15	33.07	57.29	2.40
Silt %	48.21	57.68	44.95	32.53	75.40
Clay %	10.16	19.16	21.98	10.18	22.20
Sample 2					
Sand %	11.75	16.20			
Silt %	63.15	67.20			
Clay %	25.10	16.60			
Sample 3					
Sand %	3.39	3.40	2.59	1.99	
Silt %	62.48	68.40	69.26	69.92	
Clay %	34.13	28.20	28.14	28.09	
Sample 4					
Sand %	4.78				
Silt %	61.16				
Clay %	34.06				
Sample 5					
Sand %	6.77	23.71	0.40	4.40	
Silt %	47.21	48.21	47.71	49.40	
Clay %	46.02	28.09	51.89	46.20	
Sample 6					
Sand %	7.40	25.70	84.66		
Silt %	52.40	49.20	5.18		
Clay %	40.20	25.10	10.16		

The resonant frequencies reproduce similar trend in inverted stratigraphic layers. The shallower depth inversions are interpreted as separate stratigraphic layers composed of different facies (Fig. 10b). The variation in resonant frequency to the south and north images wedged stratigraphic bodies that seem to join at the center of the array. The inverse relationship between frequency and thickness of the geologic body, suggests a stratigraphic boundary at approximately 1000 m depth.

The east-west nodes (node 1001–1021) show less variation in resonant frequencies, with the higher resonance frequency ranging between 6 and 8 Hz across the array. Only two sets of resonate frequency are apparent in the west-east nodes (Fig. 11d), with the low frequency ranging between 0.45 and 2 Hz for each node. This mirrors the resonant frequency of the centrally-located nodes in the north-south array.

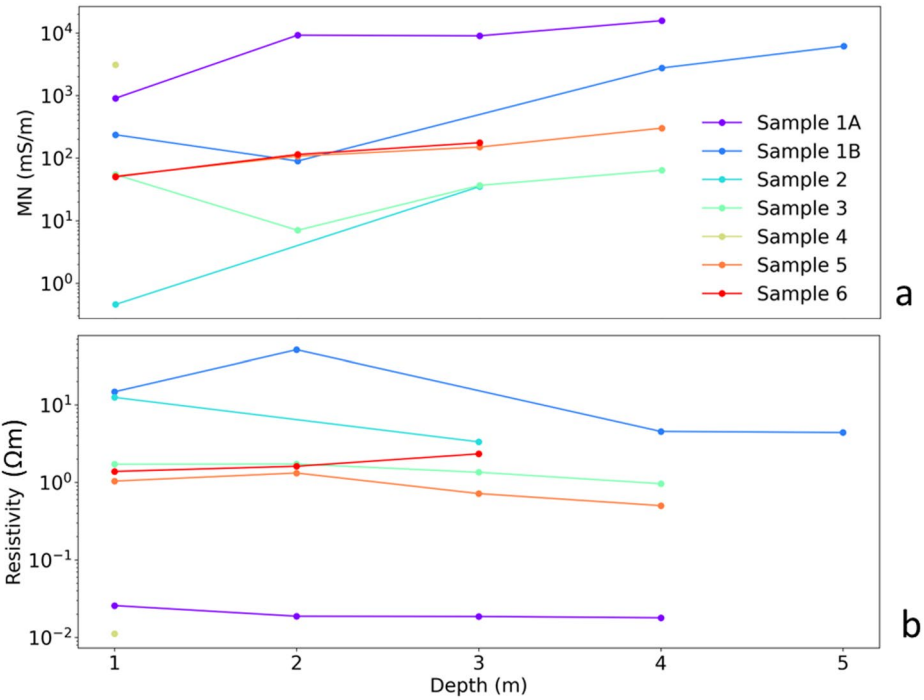

Fig. 9 Normalized chargeability **a** and resistivity **b** results from laboratory testing

5 Discussion

5.1 ERT/IP findings and interpretations

The geologic map (Fig. 1) of the region suggests that the alluvial deposits only exist very close to the Canadian River in the southern part of the study area (Moreno 2012) where we collected Lines 1 through 3. According to Heran et al. 2003; these deposits mainly consist of sand which usually appear as resistive features with low *MN* values in ERT/IP surveys (Akhtar et al. 2021; Binley and Slater 2020; Lesmes and Frye 2001; Lesmes and Morgan 2001). The grain size analysis (Table 2) of Samples 1 A and 1B show high sand content (>50%) for the surface deposits at the regions where ERT results show high resistivity values (Fig. 5), and IP surveys show low *MN* values (Fig. 7). Therefore, we assume that the resistive features with low values of *MN* appearing at depths below our coring limit are made of similar materials. With this assumption, the thin resistive layer with low *MN*, which exists at ~15 m in Line 1 and completely disappears towards the north in Line 3, is consistent with alluvial deposits in the study area that are within proximity of the Canadian River (Fig. 1), the source of these deposits (Moreno 2012). Towards the end of Line 3 the surface exhibits low resistivity, marking the end of surficial alluvium deposits. As we move to Line 4, the low resistivity features become more prominent (Fig. 6). These features also show low *MN* values (Fig. 8). We conclude that at this stage we are in the Oscars Group (Fig. 1). An extensive layer with low resistivity and high *MN* consistently exists at depth of

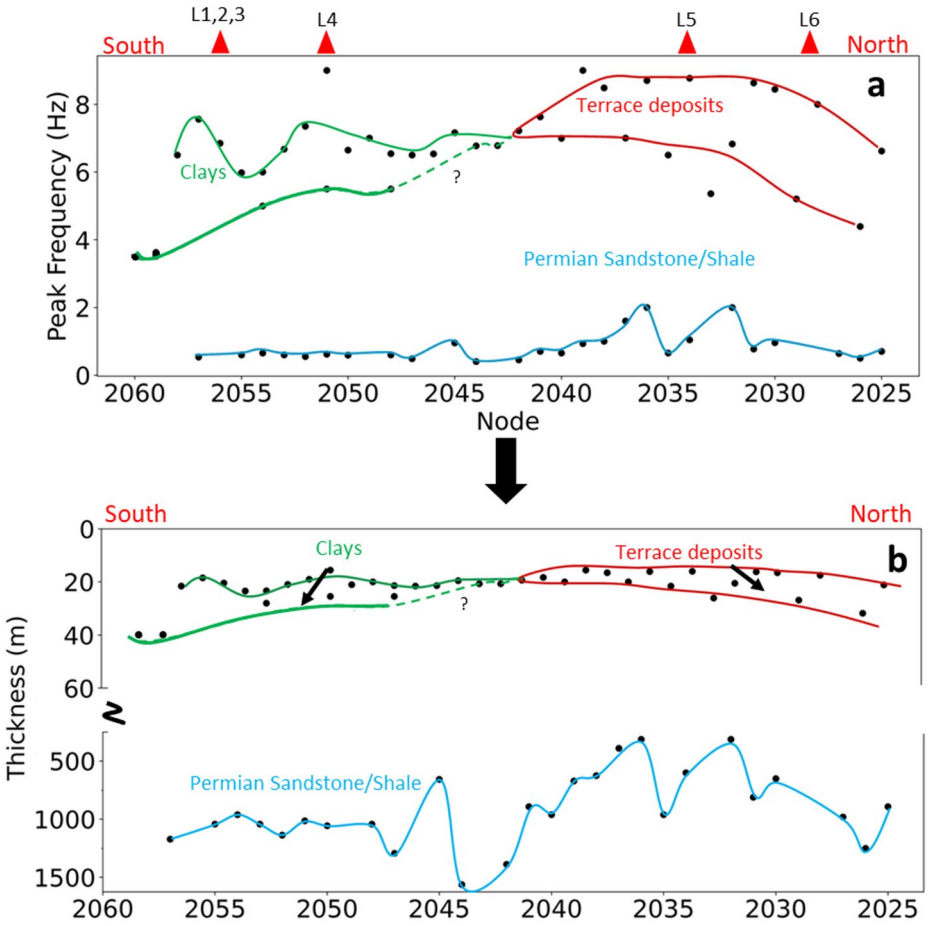

Fig. 10 Spatial mapping of the selected resonance frequencies **a** and the inverted depths of the subsurface source horizons of the resonance **b** from the north-south nodal array. The bottom axis denotes the nodal number referenced in Fig. 9. The red triangles in **a** denote the extrapolated spatial location of the ERT/IP survey lines with respect to the nodal survey. The solid lines connect interpreted resonance horizons with question marks at points of no coherent connection

~25 m in Lines 1 through 4 (marked in between red dashed lines – Figs. 5, 6, 7 and 8). This zone, reaching depths of up to 45 m, is unlikely connected to the Canadian River depositional system due to the Oscar Group reaching deeper depths than the alluvium (Heran et al. 2003). The high *MN* in this zone is due to high clay content (Binley and Slater 2020; Lesmes and Frye 2001; Slater and Lesmes 2002b), as evident by grain size analyses. In contrast, low resistivity/high *MN* features are notably absent in Lines 5 and 6 at a similar depth and it appears that these features have been replaced by high resistivity features with low *MN* values (marked between red dashed lines in Figs. 6 and 8). The high resistivity feature is laterally extensive and covers the entire Line 5, reaching to the middle of line 6. In Fig. 1, the feature aligns well with the surficial deposits map and corresponds to terrace deposits. Furthermore, grain size analyses and laboratory electrical testing further supports the identification of the feature as terrace deposits, consisting of mainly sand (Table 2). For both

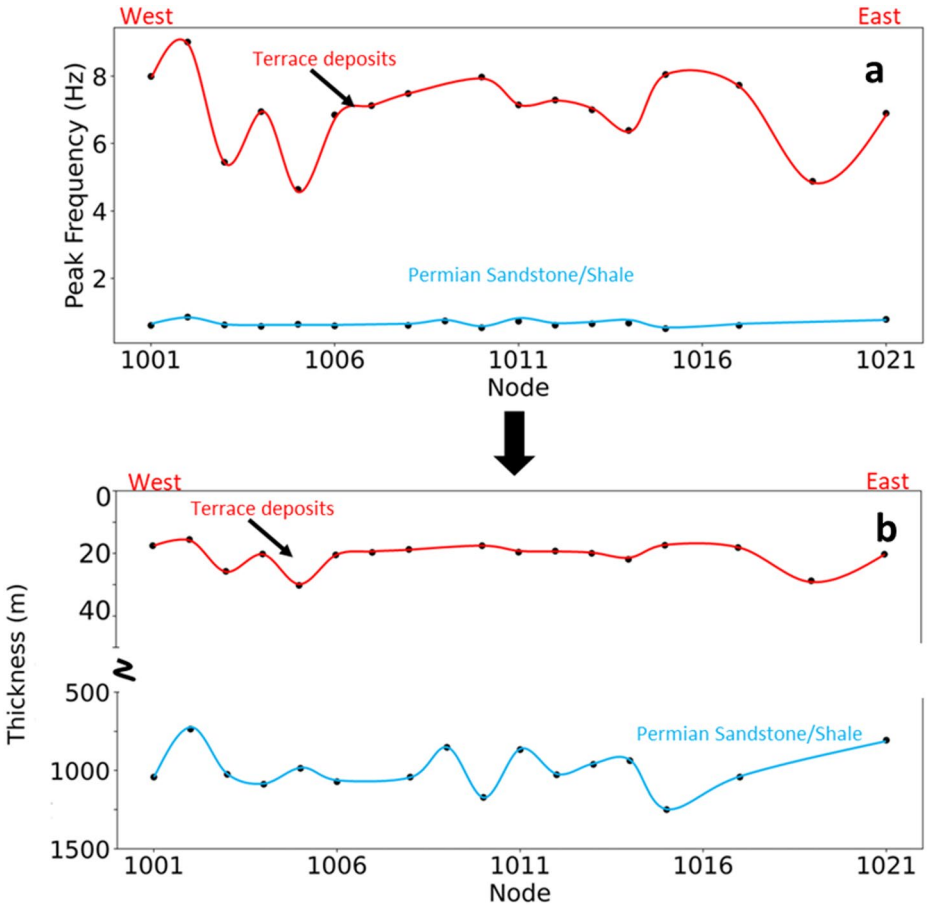

Fig. 11 Spatial mapping of the selected resonance frequencies **a** and the inverted depths of the subsurface source horizons of the resonance **b** from the west-east nodal array. The bottom axis denotes the nodal number referenced in Fig. 9. The solid lines connect interpreted resonance horizons

Lines 5 and 6, below this laterally extensive high resistivity feature (i.e., terrace deposits), the resistivity decreases to very low values, whereas *MN* increases. In Line 5, two small lobes of higher *MN*, indicative of higher clay and silt content, are observed which seem to continue into in Line 6. However, this region is very close to the depth of investigation (DOI) limit, which makes it difficult to confidently interpret the signal.

5.2 Passive seismic (HVSR) and surficial geology influence

There are noticeable spatial trends in the HVSR results of north-south passive seismic surveys (Fig. 10) that directly correlate to the electrical surveys, grain size analysis, and laboratory results. The alternating deposition strata of varying clay, sand and alluvial content produces variations in impedance contrast, thus providing strata boundaries that excite seismic resonance. The northern nodes exhibit resonant frequencies whose depth inversion correlates with strata with substantial sand content in the terrace deposits in that region, as

revealed in the ERT/IP Lines 5 and 6. The depth of the sandy deposits aligns well with ERT/IP survey Lines 5 and 6, using the reference shear wave velocity of 560 m/s (Mendoza et al. 2017). Lines 5 and 6 show the depth of the sandy layer ~ 25 m in the north, which matches with the HVSR results for the red horizon (Fig. 10) in the northern nodes. The terrace deposits seem to thin towards the center of the array and widen while dipping to the north.

The southern nodes image deeper strata compared to the northern nodes. The southern node resonant frequency analysis also suggests deeper structures that are evident in the ERT/IP Lines 1 through 3. The green horizon bounds a stratum rich in clay that is overlain by alluvial deposits. This change in strata composition provides a change in impedance contrast resulting in seismic signal resonance. The clay strata are thicker and dip towards the Canadian River. The layer seems to truncate towards the center of the north array. The east-west array samples an area that is subparallel to the river channel and a zone that is devoid of the clay strata. This is apparent across the array and may mark the edge of deposition by the current or recent (since the Holocene) river channel. We note, using the current data, we are not able to resolve depositions that constitute gradual change in strata composition.

The deeper blue horizon in the two arrays cannot be imaged using the ERT/IP method. The horizon at approximately 1 km depth corresponds to the transition between Permian and Pennsylvanian deposits (*Geologic Units in Canadian County*, *Oklahoma*, 2024). This zone is composed of a series of sandstone and shale strata that produce high impedance contrast at the strata boundaries, resulting in seismic wave resonance. While the nodes have a natural frequency of 5 Hz, the combined application of signal ratios and high impedance contrast enhances the resonant signal thereby enabling the imaging using the lower frequencies (<2 Hz).

We identified borehole descriptions from water wells in the area, though they lacked the accuracy and detail necessary for inclusion in our geophysical analysis. Additionally, well log data, including resistivity information, was unavailable, as logging does not usually occur until deeper depths are reached into known oil-bearing zones. Thus, these techniques may be important for characterizing near-surface zones. Nonetheless, shallow direct sampling in this study proved valuable as ground truth. While the nodal spacing in passive seismic surveys allowed extensive coverage here, future work with a denser nodal array may help refine the imaging of the subsurface strata, particularly in the north-south array of the study area. In the context of in-situ sampling, additional geotechnical parameters could complement the methods outlined here.

6 Conclusion

This study effectively combines elements of electrical and passive seismic geophysical methods to spatially characterize near-surface structures that heighten seismic hazard. Despite a decrease in the occurrence of large-magnitude induced earthquakes in Oklahoma since 2016, small-magnitude induced seismicity remains frequent with amplified amplitude due to seismic wave resonance. The nodal data provides valuable insights into deeper near-surface structures that originate seismic wave resonance. The combined results of electrical and passive seismic surveys with in-situ sampling, and laboratory testing unveil near-surface features that amplify induced seismic energy. Specifically, ERT/IP surveys, with the help of in-situ sampling, precisely delineate the spatial distribution of near-surface materials

such as the Canadian River alluvium, terrace deposits and clayey layers, and assist in interpretation of the passive seismic imaging.

Seismic energy amplification from crustal reverberations is governed by impedance contrasts and the resonance conditions of layered sediments. When coarse-grained units such as sands or gravels are interbedded with finer-grained deposits like silts or clays, the strong acoustic impedance contrast at these interfaces causes partial reflection and constructive interference of seismic waves. Amplification is most pronounced when the thickness of a sedimentary layer approximates one-quarter of the dominant seismic wavelength (the quarter-wavelength resonance condition), which typically corresponds to shallow depths on the order of 10–30 m for frequencies between 2 and 10 Hz common in near-surface site response (Bard and Bouchon 1985; Kramer 1996). Thus, layering within the upper 20 m is particularly critical, since it coincides with frequencies that control ground shaking intensity and potential damage (Field 1996). At greater depths, resonance can still occur if thick, low-velocity layers underlie higher-velocity material, producing fundamental frequencies that may overlap with the energy band of regional seismic sources. Our multi-method investigation highlights these conditions by demonstrating how specific combinations of sediment velocity, thickness, and depth contribute to reverberations that amplify seismic energy. We suggest that earthquake hazard maps should always consider the potential increased level of risk from overlapping sedimentary depositions across the state of Oklahoma.

Acknowledgements We thank Dr. Caitlin Hodges for providing guidance on grain size analysis.

Funding This study and all authors have received no funding.

Declarations

Competing Interests The authors have no competing interests to declare that are relevant to the content of this article.

References

Akhtar N, Mislan MS, Syakir MI, Anees MT, Yusuff MSM (2021) Characterization of aquifer system using electrical resistivity tomography (ERT) and induced polarisation (IP) techniques. IOP Conference Series: Earth and Environmental Science, 880(1), 012025. https://doi.org/10.1088/1755-1315/880/1/012025

Arimuko A, Santoso E, Sunardi B (2020) Investigation of site condition using elliptical curve inversion from Horizontal-to-Vertical spectral ratio (HVSR). J Phys: Conf Ser 1491(1):012031. https://doi.org/10.1088/1742-6596/1491/1/012031

Atkinson GM (2020) The intensity of ground motions from induced earthquakes with implications for damage potential. Bull Seismol Soc Am 110(5):2366–2379. https://doi.org/10.1785/0120190166

Bard PY, Bouchon M (1985) The two-dimensional resonance of sediment-filled valleys. Bull Seismol Soc Am 75(2):519–541
Binley A, Slater L (2020) Resistivity and induced polarization: theory and applications to the Near-Surface Earth. Cambridge University Press. https://doi.org/10.1017/9781108685955
Blanchy G, Saneiyan S, Boyd J, McLachlan P, Binley A (2020) ResIPy, an intuitive open source software for complex geoelectrical inversion/modeling. Comput Geosci 137:104423. https://doi.org/10.1016/j.cageo.2020.104423
Boyd J, Blanchy G, Saneiyan S, McLachlan P, Binley A (2019) 3D geoelectrical problems with ResiPy, an open source graphical user interface for geoelectrical data processing. https://doi.org/10.13140/RG.2.2.35381.63205
Breit GN, Tuttle MLW, Cozzarelli IM, Berry CJ, Christenson SC, Jaeschke JB (2008) Results of the chemical and isotopic analyses of sediment and ground water from alluvium of the Canadian River near a closed municipal landfill, Norman, Oklahoma, part 2. In Results of the chemical and isotopic analyses of sediment and ground water from alluvium of the Canadian River near a closed municipal landfill, Norman, Oklahoma, part 2 (USGS Numbered Series 2008–1134; Open-File Report, Vols. 2008–1134). U.S. Geological Survey. https://doi.org/10.3133/ofr20081134
Carter BJ, Gregory MS (2008) Soil Map of Oklahoma [Map]. Department of Plant and Soil Sciences, Oklahoma State University. http://www.ogs.ou.edu/pubsscanned/EP9p16_19soil_veg_cl.pdf
Cheng T, Cox BR, Vantassel JP, Manuel L (2020) A statistical approach to account for azimuthal variability in single-station HVSR measurements. Geophys J Int 223(2):1040–1053. https://doi.org/10.1093/gji/ggaa342
Cheung R, Wetherell D, Whitaker S (2018) Induced earthquakes and housing markets: evidence from Oklahoma. Reg Sci Urban Econ 69:153–166. https://doi.org/10.1016/j.regsciurbeco.2018.01.004
Cox BR, Cheng T, Vantassel JP, Manuel L (2020) A statistical representation and frequency-domain window-rejection algorithm for single-station HVSR measurements. Geophys J Int 221(3):2170–2183. https://doi.org/10.1093/gji/ggaa119
Curtis JA (2003) Geomorphic and hydrologic assessment of erosion hazards at the Norman municipal Landfill, Canadian river Floodplain, central Oklahoma. Environ Eng Geosci 9(3):241–253. https://doi.org/10.2113/9.3.241
Eaton DW, Schultz R (2018) Increased likelihood of induced seismicity in highly overpressured shale formations. Geophys J Int 214(1):751–757. https://doi.org/10.1093/gji/ggy167
Field EH (1996) Spectral amplification in a sediment-filled Valley exhibiting clear basin-edge-induced waves. Bull Seismol Soc Am 86(4):991–1005
Geologic units in Canadian county, Oklahoma. (2024) USGS. https://mrdata.usgs.gov/geology/state/fips-unit.php?code=f40017
Giocoli A, Hailemikael S, Bellanova J, Calamita G, Perrone A, Piscitelli S (2019) Site and Building characterization of the Orvieto Cathedral (Umbria, central Italy) by electrical resistivity tomography and single-station ambient vibration measurements. Eng Geol 260:105195. https://doi.org/10.1016/j.enggeo.2019.105195
GISGeography (2024) Oklahoma Outline Map. https://gisgeography.com/wp-content/uploads/2020/03/Oklahoma-Outline-Map.jpg
Havens JS (1989) Geohydrology of the alluvial and terrace deposits of the North Canadian River from Oklahoma City to Eufaula Lake, central Oklahoma. In Geohydrology of the alluvial and terrace deposits of the North Canadian River from Oklahoma City to Eufaula Lake, central Oklahoma (USGS Numbered Series 88–4234; Water-Resources Investigations Report, Vols. 88–4234). U.S. Geological Survey; Books and Open-file reports, Federal Center,. https://doi.org/10.3133/wri884234
Heran WD, Green GN, Stoeser DB (2003) A digital geologic map database for the state of Oklahoma (Report 2003–247; Version 1.1, Open-File Report). USGS Publications Warehouse. https://doi.org/10.3133/ofr03247
Hesaraki S, Zamanian A, Moztarzadeh F (2009) Effect of adding sodium hexametaphosphate liquefier on basic properties of calcium phosphate cements. J Biomedical Mater Res Part A 88A(2):314–321. https://doi.org/10.1002/jbm.a.31836
Hincks T, Aspinall W, Cooke R, Gernon T (2018) Oklahoma's induced seismicity strongly linked to wastewater injection depth. Science 359(6381):1251–1255. https://doi.org/10.1126/science.aap7911
Vantassel J (2021) Hvsrpy: V1.0.0. https://doi.org/10.5281/zenodo.5563211
Kemna A, Binley A, Cassiani G, Niederleithinger E, Revil A, Slater L, Williams KH, Orozco AF, Haegel F-H, Hördt A, Kruschwitz S, Leroux V, Titov K, Zimmermann E (2012) An overview of the spectral induced polarization method for near-surface applications. Near Surf Geophys 10(6):453–468. https://doi.org/10.3997/1873-0604.2012027
Kramer SL (1996) Geotechnical earthquake engineering. Prentice Hall, Upper Saddle River, NJ

Lesmes DP, Frye KM (2001) Influence of pore fluid chemistry on the complex conductivity and induced polarization responses of berea sandstone. J Geophys Research: Solid Earth 106(B3):4079–4090. https://doi.org/10.1029/2000JB900392

Lesmes DP, Morgan FD (2001) Dielectric spectroscopy of sedimentary rocks. J Geophys Research: Solid Earth 106(B7):13329–13346. https://doi.org/10.1029/2000JB900402

Leyton F, Ruiz S, Sepúlveda SA, Contreras JP, Rebolledo S, Astroza M (2013) Microtremors' HVSR and its correlation with surface geology and damage observed after the 2010 Maule earthquake (Mw 8.8) at Talca and Curicó, central Chile. Eng Geol 161:26–33. https://doi.org/10.1016/j.enggeo.2013.04.009

Mahajan AK, Kumar P, Kumar P (2021) Near-surface seismic site characterization using Nakamura-based HVSR technique in the geological complex region of Kangra Valley, Northwest Himalaya, India. Arab J Geosci 14(10):826. https://doi.org/10.1007/s12517-021-07136-w

McNamara DE, Benz HM, Herrmann RB, Bergman EA, Earle P, Holland A, Baldwin R, Gassner A (2015) Earthquake hypocenters and focal mechanisms in central Oklahoma reveal a complex system of reactivated subsurface strike-slip faulting. Geophys Res Lett 42(8):2742–2749. https://doi.org/10.1002/2014GL062730

Mendoza C, Turner J, O'Connell D (2017) Ground motion characterization and Site- Specific IMASW Vs-depth measurements at CEUS Seismic Stations: The 2011 Prague, OK Earthquake

Moreno MA (2012) Middle Canadian, Lower Canadian, & Little River Basins

Mulargia F, Castellaro S (2016) HVSR deep mapping tested down to ∼1.8 Km in Po plane Valley, Italy. Phys Earth Planet Inter 261:17–23.

Murray KE, Brooks C, Walter JI, Ogwari PO (2023) Oklahoma's coordinated response to more than a decade of elevated seismicity. GSA Special Paper 559 Recent Seismicity South Midcontinent USA: Sci Regul Ind Responses. https://doi.org/10.1130/2023.2559

Nakamura Y (2019) What is the Nakamura method? Seismol Res Lett 90(4):1437–1443. https://doi.org/10.1785/0220180376

Nakamura YA (1989) Method for dynamic characteristics estimation of subsurface, using microtremor on the ground surface. Railway Technical Research Institute. Quarterly Rep. 30(1). https://trid.trb.org/view/294184

Ogwari P, Walter JI, Chen X, Thiel A, Ferrer F, Woelfel I (2022) Distinguishing unique earthquakes with overlapping signals in Oklahoma. Seismol Res Lett 93(6):3384–3395. https://doi.org/10.1785/0220220065

Oubaiche EH, Chatelain J, Hellel M, Wathelet M, Machane D, Bensalem R, Bouguern A (2016) The relationship between ambient vibration H/V and SH transfer function: some experimental results. Seismol Res Lett 87(5):1112–1119. https://doi.org/10.1785/0220160113

Ries R, Brudzinski MR, Skoumal RJ, Currie BS (2020) Factors influencing the probability of hydraulic Fracturing-Induced seismicity in Oklahoma. Bull Seismol Soc Am 110(5):2272–2282. https://doi.org/10.1785/0120200105

Schoenball M, Ellsworth WL (2017) A systematic assessment of the Spatiotemporal evolution of fault activation through induced seismicity in Oklahoma and Southern Kansas. J Geophys Research: Solid Earth 122(12):10189–10206. https://doi.org/10.1002/2017JB014850

Sivaram K, Gupta S, Kumar S, Prasad BNV (2018) Shear velocity structural characterization around the Lonar crater using joint inversion of ambient noise HVSR and Rayleigh wave dispersion. J Appl Geophys 159:773–784. https://doi.org/10.1016/j.jappgeo.2018.10.022

Slater LD, Lesmes D (2002a) IP interpretation in environmental investigations. Geophysics 67(1):77–88. https://doi.org/10.1190/1.1451353

Slater LD, Lesmes D (2002b) IP interpretation in environmental investigations. Geophysics 67(1):77. https://doi.org/10.1190/1.1451353

Stanko D, Markušić S, Strelec S, Gazdek M (2017) HVSR analysis of seismic site effects and soil-structure resonance in Varaždin City (North Croatia). Soil Dyn Earthq Eng 92:666–677. https://doi.org/10.1016/j.soildyn.2016.10.022

Taylor O-DS, Lester AP, Lee TA, McKenna MH (2018) Can repetitive small Magnitude-Induced seismic events actually cause damage? Adv Civil Eng 2018:2056123. https://doi.org/10.1155/2018/2056123

Tuttle MLW, Breit GN, Cozzarelli IM (2009) Processes affecting δ34S and δ18O values of dissolved sulfate in alluvium along the Canadian River, central Oklahoma, USA. Chem Geol 265(3):455–467. https://doi.org/10.1016/j.chemgeo.2009.05.009

USGS Earthquake Catalog (2024) USGS. https://earthquake.usgs.gov/earthquakes/search/

Walter JI, Ogwari P, Thiel A, Ferrer F, Woelfel I, Chang JC, Darold AP, Holland AA (2019) The Oklahoma geological survey statewide seismic network. Seismol Res Lett 91(2A):611–621. https://doi.org/10.1785/0220190211

Ward SH (1990) Resistivity and induced polarization methods | geotechnical and environmental geophysics: I, review and tutorial. Investigations Geophys Ser 147–190. https://doi.org/10.1190/1.9781560802785.ch6

Waxman MH, Smits LJM (1968) Electrical conductivities in oil-bearing Shaly sands. Trans Am Inst Mineral Metall Petrol Eng 243(2):107–122. https://doi.org/10.2118/1863-A

Zhai G, Shirzaei M, Manga M, Chen X (2019) Pore-pressure diffusion, enhanced by poroelastic stresses, controls induced seismicity in Oklahoma. Proc Natl Acad Sci 116(33):16228–16233. https://doi.org/10.1073/pnas.1819225116